Published in "Physical Chemistry Chemical Physics19(31): 20919–20929, 2017"
which should be cited to refer to this work.

A non-empirical calculation of 2p core-electron excitation in compounds with 3d transition metal ions using ligand-field and density functional theory (LFDFT)†

Harry Ramanantoanina *[a] and Claude Daul[b]

Methodological advents for the calculation of the multiplet energy levels arising from multiple-open-shell $2p^53d^{n+1}$ electron configurations, with n = 0, 1, 2,... and 9, are presented. We use the Ligand-Field Density Functional Theory (LFDFT) program, which has been recently implemented in the Amsterdam Density Functional (ADF) program package. The methodology consists of calculating the electronic structure of a central metal ion together with its ligand coordination by means of the Density Functional Theory code. Besides, the core-hole effects are treated by incorporating many body effects and corrections *via* the configuration interaction algorithm within the active space of Kohn–Sham orbitals with dominant 2p and 3d characters of the transition metal ions, using an effective ligand-field Hamiltonian. The Slater–Condon integrals (F^2(3d,3d), F^4(3d,3d), G^1(2p,3d), G^3(2p,3d) and F^2(2p,3d)), spin–orbit coupling constants (ζ_{2p} and ζ_{3d}) and parameters of the ligand-field potential (represented within the Wybourne formalism) are therefore determined giving rise to the multiplet structures of systems with $3d^n$ and $2p^53d^{n+1}$ configurations. The oscillator strengths of the electric-dipole allowed $3d^n \rightarrow 2p^53d^{n+1}$ transitions are also calculated allowing the theoretical simulation of the absorption spectra of the 2p core-electron excitation. This methodology is applied to transition metal ions in the series Sc^{2+}, Ti^{2+},..., Ni^{2+} and Cu^{2+} but also to selective compounds, namely $SrTiO_3$ and MnF_2. The comparison with available experimental data is good. Therefore, a non-empirical ligand-field treatment of the $2p^53d^{n+1}$ configurations is established and available in the ADF program package illustrating the spectroscopic details of the 2p core-electron excitation that can be valuable in the further understanding and interpretation of the transition metal $L_{2,3}$-edge X-ray absorption spectra.

Introduction

LFDFT is the acronym for Ligand-Field Density Functional Theory. It is a quantum chemistry based method that calculates the electronic structure and properties associated with multiple-open-shell electron configurations in metal ions. Initiated in Fribourg in Switzerland,[1–3] its development was successful due to the contribution and expertise of many scientists from many European workplaces.[1–15] LFDFT is a fully non-empirical method, in which the ligand-field parameters (Slater–Condon integrals, spin–orbit coupling constants and ligand-field potential) are extracted from the output of a conceptual theoretical procedure.[1–15] LFDFT results are achieved with two important steps: first theoretical calculation based on a molecular cluster system by means of the Density Functional Theory code (DFT); and second post-computational analysis with our ligand-field module, which employs tools established using the crystal-/ligand-field model[16–19] and molecular orbital theory. By means of LFDFT, the multiplet energy levels associated with a given electron configuration are determined, important for further description of the magnetic and optical properties of metal compounds. Based on very encouraging LFDFT results obtained for the last two decades (a non-exhaustive list of reportable applications could be found in ref. 1–15 and 20–25), we have implemented the LFDFT method into the Amsterdam Density Functional (ADF) program package (ADF2017.103),[26–28] with relevance for calculation of the electronic fine structure of systems with p^n, d^n, f^n and f^nd^1 electron configurations, for an integer value of n.

[a] *Paul Scherrer Institute, CH-5232 Villigen, Switzerland.*
E-mail: harry.ra@hotmail.com
[b] *Department of Chemistry, University of Fribourg, Chemin du Musée 9, CH-1700 Fribourg, Switzerland*

† Electronic supplementary information (ESI) available: A comparative view of the LFDFT results of the absorption spectra due to the $3d^n \rightarrow 2p^53d^{n+1}$ transitions of Mn^{2+}, M n^{3+} and Mn^{4+}, with n = 5, 4 and 3, respectively; a graphical representation of the impact of the DFT functional on the LFDFT results of Mn^{2+}; calculated radial functions of the Kohn–Sham orbitals with dominant 3d characters of Mn^{2+} in the molecular $(MnF_6)^{4-}$ cluster within the $3d^5$ and $2p^53d^6$ electron configurations.

In this work, the scope of LFDFT is extended to account for the final electronic states of metal compounds under core-electron excitation processes. An aspect of materials characterization is nowadays obtained using core-electron excitation analysis, popularized by analytical tools such as X-ray absorption spectroscopy and electron energy-loss spectroscopy. For instance, X-ray absorption spectroscopy has become considerably popular because of its remarkable advantages, including element specificity and local geometric and electronic structure probing.[29] Then, the use of X-ray absorption spectroscopy goes well beyond the academic interest as it offers an experimental tool capable of fundamentally understanding atoms, molecules and condensed matter.[29] The X-ray absorption experiments are frequently performed at the K- and $L_{2,3}$-edges for transition metal elements.[29–31] They correspond to the processes in which incident X-ray photons are absorbed by promoting one electron from the 1s and 2p core-orbitals, respectively, to the valence ones. In the spectra, strong features are often observed,[29,32] which represent the interaction of the core-electron with the valence ones governed by electric-dipole moment selection rules.

It is noteworthy that many theoretical methods[33–40] are frequently used for the simulation of the X-ray absorption spectra of metal compounds. Some of those methods[33,34] *a priori* utilize the principles of crystal-/ligand-field theory to solve multiplet structure problems and to simulate optical transitions in the same manner as provided by the LFDFT approach. The advantage of those methods resides with the aspects of a semi-empirical solution, which is especially developed on induction from experimental findings. But the improvement that is brought by LFDFT in the ADF program package[26–28] is a parameter-free ligand-field concept, in which the DFT code in ADF and our ligand-field module are merged in the perspective of a fully non-empirical ligand-field consideration of the electron transition processes. Herein, we present for the first time the LFDFT results for the 2p core-electron excitation in transition metal compounds. The LFDFT methodology is described. Then the results are presented with respect to the calculation of the multiplet energy levels arising from the $2p^53d^{n+1}$ electron configurations, with n = 0, 1, 2,... and 9 of divalent transition metal ions and selective compounds. The oscillator strengths of the $3d^n \rightarrow 2p^53d^{n+1}$ transitions are also calculated, allowing for a non-empirical simulation of the absorption spectra that could represent the transition metal $L_{2,3}$-edge X-ray absorption or electron energy loss spectra. Future works include the LFDFT calculation of core 4d and 4f excitations in lanthanide and actinide compounds, which will be presented and incorporated into the ADF program package.[26–28] They are important for the understanding and characterization of the lanthanide $N_{4,5}$- and actinide $N_{6,7}$-edge X-ray absorption spectra.

Methodology

In this work, we use the effective ligand-field Hamiltonian in eqn (1) to calculate the multiplet energy levels arising from a multiple-open-shell electron configuration. Eqn (1) sum up the quantum effects related to the electron-electron repulsion and exchange (H_{ER}), spin–orbit coupling interaction (H_{SO}) and ligand field splitting (H_{LF}):

$$H = H_0 + H_{ER} + H_{SO} + H_{LF} \tag{1}$$

where the matrix elements of H are expressed on the basis of single determinants of spin–orbitals (Slater-determinants), which belong to a multiple-open-shell electron configuration. More practically, we are restricted to $3d^n$ and $2p^53d^{n+1}$, with n = 0, 1,... and 9, which can represent the ground and excited electron configurations of transition metal ions in compounds under X-ray irradiation.

The diagonalization of H yields eigenvalues also known as multiplet energy levels that can be used to characterize the electronic fine structure of the systems under investigation. The term for the electron–electron repulsion and exchange in eqn (1) is based on the central-field approximation and perturbation theory of Slater:[41,42]

$$\begin{aligned} H_{ER} = &\sum_{k=2,4} F^k(3d,3d) f_k(dd) + F^2(2p,3d) f_2(pd) \\ &+ \sum_{k=1,3} G^k(2p,3d) g_k(pd) \end{aligned} \tag{2}$$

where the matrix elements of H_{ER} are constructed in terms of the Slater–Condon F and G integrals representing the Coulomb and exchange interactions, respectively; and the angular coefficients f and g.[41,42]

In LFDFT, the Slater–Condon F and G integrals are calculated non-empirically with the radial functions R_{3d} and R_{2p} extracted from the Kohn–Sham orbitals with dominant 2p and 3d characters of the transition metal ions (eqn (3)–(5)).

$$F^k(3d,3d) = \int_0^\infty \int_0^\infty \frac{r_<^k}{r_>^{k+1}} R_{3d}{}^2(r_1) R_{3d}{}^2(r_2) r_1{}^2 r_2{}^2 dr_1 dr_2 \tag{3}$$

$$F^2(2p,3d) = \int_0^\infty \int_0^\infty \frac{r_<^2}{r_>^3} R_{2p}{}^2(r_1) R_{3d}{}^2(r_2) r_1{}^2 r_2{}^2 dr_1 dr_2 \tag{4}$$

$$G^k(2p,3d) = \int_0^\infty \int_0^\infty \frac{r_<^k}{r_>^{k+1}} R_{2p}(r_1) R_{3d}(r_2) R_{3d}(r_1) R_{2p}(r_2) r_1{}^2 r_2{}^2 dr_1 dr_2 \tag{5}$$

The radial functions are conventionally expanded with respect to Slater-type orbital (STO) functions in the ADF program package (see also Fig. 1).[26–28] In eqn (3)–(5), $r_<$ and $r_>$ are the lesser and greater of the distances r_1 and r_2 of two electrons from the nucleus.

Note that in eqn (2), the terms corresponding to the zeroth-order Slater–Condon integrals (F^0(2p,3d), F^0(2p,2p) and F^0(3d,3d)) are dropped, because they are engulfed in the term H_0 in eqn (1), which can be represented with a diagonal matrix:

$$H_0 = \begin{pmatrix} I_{N(3d^n)} \cdot 0 & (0) \\ (0) & I_{N(2p^53d^{n+1})} \cdot \Delta \end{pmatrix} \tag{6}$$

where, the parameter Δ corresponds to the difference of the configuration-average energies between $2p^53d^{n+1}$ and $3d^n$; I_N is an identity matrix of rank N; and N represents the dimension of

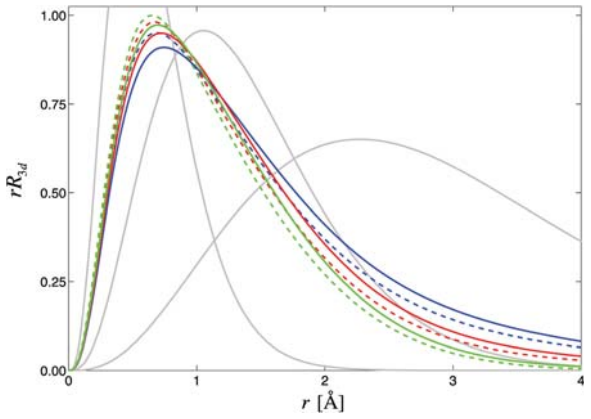

Fig. 1 Graphical representation of the 3d radial functions of Mn^{2+} (in blue), Mn^{3+} (in red) and Mn^{4+} (in green) within the $3d^n$ (solid curve) and $2p^53d^{n+1}$ (dashed curve) electron configurations, with n = 5, 4 and 3. The grey curves represent three Slater-type orbital functions from which the radial functions are expanded.

the Hilbert space given by the total number of single determinants of spin–orbitals arising from the multiple-open-shell electron configuration. N is analytically expressed by the mathematical combinatorial formula in terms of the integer n:

$$N(3d^n) = \binom{10}{n} \tag{7}$$

and

$$N(2p^53d^{n+1}) = \binom{6}{5}\binom{10}{n+1} \tag{8}$$

In LFDFT, the parameter Δ is calculated as follows:

$$\Delta = E^{DFT}(2p^53d^{n+1}) - E^{DFT}(3d^n) \tag{9}$$

where, $E^{DFT}(2p^53d^{n+1})$ and $E^{DFT}(3d^n)$ are the total electronic energies obtained from the DFT calculations for the system having $2p^53d^{n+1}$ and $3d^n$ electron configurations of the transition metal ions. Aside from the zeroth-order inter-electronic repulsion interaction parameters (F^0(2p,3d), F^0(2p,2p) and F^0(3d,3d)), Δ in principle combines many quantities, for instance: the one-electron terms corresponding to the kinetic energy background and nuclear-electron attraction; as well as the parameters B_0^0(2p,2p) and B_0^0(3d,3d) for the ligand field potential, which will be discussed in another paragraph. Note however that all these quantities cannot be discriminated separately from the LFDFT calculations.

The term for the spin–orbit coupling interaction in eqn (1) is represented by a sum of one-electron spin–orbit contributions, which describes the interaction of the spin of an electron i on the atom, only with the angular momentum of its own orbital:

$$H_{SO} = \sum_i \zeta_{n_i l_i}(r_i)(l_i \cdot s_i) \tag{10}$$

where $\zeta_{nl}(r)$ is an operator that describes the radial part of the spin–orbit coupling; $l_i{\cdot}s_i$ describes the coupling of the angular momenta of the spin and orbit, respectively.

Owing to the fact that the radial part can be factored out in eqn (10), the spin–orbit coupling constant ζ_{nl} can be obtained in two different ways. We use the first calculation route in LFDFT, using the radial functions R_{nl} as follows:

$$\zeta_{nl} = \frac{\alpha^2}{2}\int_0^\infty \frac{1}{r}\left(\frac{dV}{dr}\right)|R_{nl}(r)|^2 r^2 dr \tag{11}$$

where, α is the fine structure constant; and V is the central-field potential-energy function, which is approximated here with a simple coulomb potential ($-2Z/r$). The second calculation route will be described later in eqn (14).

The term for the ligand-field splitting in eqn (1) represents the contribution of the chemical environment (ligands) to the electronic structure of the transition metal ion. This is parameterized within the Wybourne formalism,[43] where the matrix elements of the ligand-field splitting Hamiltonian are obtained as the product of the Wybourne-normalized crystal field parameters B and the spherical harmonic tensor operator C acting on the 2p and 3d orbitals (eqn (12)).

$$H_{LF} = \sum_{k=0,2}\sum_{q=-k}^{k} B_q^k(2p,2p)C_q^{(k)} + \sum_{k=0,2,4}\sum_{q=-k}^{k} B_q^k(3d,3d)C_q^{(k)} + \sum_{k=1,3}\sum_{q=-k}^{k} B_q^k(2p,3d)C_q^{(k)} \tag{12}$$

The effect of the ligand field splitting Hamiltonian is with respect to symmetry constraints according to the spatial arrangement of the ligand system in the coordination sphere of the transition metal ions. In LFDFT, the parameters B are determined from the eigenfunctions and eigenvalues of the Kohn–Sham orbitals with dominant 2p and 3d characters using mathematical least squares fit.

The ultimate goal of the LFDFT program consists of producing non-empirical ligand-field parameters using a single-point DFT calculation: *i.e.* the Slater–Condon integrals by means of eqn (3)–(5); the spin–orbit coupling constants by means of eqn (11); the ligand-field potential by means of eqn (12) and the energy gap Δ (eqn (9)). Then these parameters are used to compute the multiplet energy levels that are susceptible to represent the electron configuration systems (*i.e.* $3d^n$ and $2p^53d^{n+1}$) from which eqn (1) operates.

Computational details

The LFDFT calculations have been carried out by means of the Amsterdam Density Functional (ADF) program package (ADF2017.103).[26–28] Three levels of approximation for the exchange and correlation DFT functional were used: the local density approximation (LDA) SVWN,[44] the generalized gradient approximation (GGA) PBE[45] and the hybrid B3LYP.[46] The molecular orbitals were expanded using triple-zeta Slater-type orbital (STO) functions plus one polarization extra function (TZP)[47] for the transition metal elements and double-zeta STO functions plus one polarization extra function (DZP)[47] for other

elements. The self-consistent field (SCF) was set-up to take into account all electrons. The relativistic corrections were treated with the Zeroth-order Regular Approximation (ZORA) of the Dirac equation method as implemented in the ADF program package.[26–28] The scalar and spin–orbit parts of the ZORA Hamiltonian were used to provide an accurate description of both the spin-independent and spin-dependent relativistic effects. The results were achieved using the recently available ''LFDFT'' and ''LFDFT_TDM'' keywords in the ADF program package,[26–28] which enable calculation of multiplet energy levels and oscillator strengths of electronic transitions.

The LFDFT method consists of performing a single-point DFT calculation with the average of the configuration (AOC) scheme[1,14,15] for the electron population in order to represent the systems of electron configurations under investigation: $3d^n$ and $2p^5 3d^{n+1}$, with n = 0, 1, 2,. . ., and 9 in transition metal ions. It is a restricted SCF calculation, without symmetry constraint, where the Kohn–Sham orbitals assimilated with dominant 2p and 3d characters are populated with fractional electrons controlled *via* the ''OCCUPATION'' keyword available in the ADF program package.[26–28] For example: a DFT calculation with a $3d^n$ configuration is achieved by occupying with $n/5$ electrons the five-fold Kohn–Sham orbitals assimilated with a dominant 3d character; on the other hand, a DFT calculation with the $2p^5 3d^{n+1}$ configurations is achieved by occupying with 5/3 and $(n + 1)/5$ electrons the Kohn–Sham orbitals assimilated with dominant 2p and 3d characters, respectively. Thus, the electron density belongs to the totally symmetric representation under which the operating effective ligand-field Hamiltonian (eqn (1)) is invariant. Besides, the concept of LFDFT consists of treating explicitly the near degeneracy correlation using the configuration interaction algorithm within the restricted active subspace of the Kohn–Sham orbitals constructed earlier from DFT,[1,14,15] by means of the effective ligand-field Hamiltonian.

Results and discussion

It is important to start this section with discussion about the radial functions of atomic orbitals, from which the Slater–Condon integrals and spin–orbit coupling constants are calculated in LFDFT using eqn (3)–(5) and (11), respectively. Fig. 1 shows examples of calculated radial functions corresponding to the 3d Kohn–Sham orbitals of Mn ions. The calculations are performed

Table 1 LFDFT parameters (in eV) corresponding to the $3d^n$ (GS) and $2p^5 3d^{n+1}$ (ES) electron configurations of free Ca^{2+}, Ti^{4+}, Sc^{2+}, Ti^{2+}, V^{2+}, Mn^{4+}, Cr^{2+}, Mn^{3+}, Mn^{2+}, Fe^{2+}, Co^{2+}, Ni^{2+} and Cu^{2+} ions, with n = 0, 0, 1, 2, 3, 3, 4, 4, 5, 6, 7, 8 and 9, respectively, by means of DFT calculation employing the LDA, GGA and hybrid functional; together with some reference values (Ref.) taken from the literature

		GS			ES							
		F^2(3d,3d)	F^4(3d,3d)	ζ_{3d}	Δ	F^2(3d,3d)	F^4(3d,3d)	G^1(2p,3d)	G^3(2p,3d)	F^2(2p,3d)	ζ_{2p}	ζ_{3d}
Ca^{2+}	GGA	—	—	—	350.37	—	—	2.024	1.161	3.389	2.521	0.011
	Ref.[a]	—	—	—	350.37	—	—	2.51	1.42	3.79	2.4	0.011
Ti^{4+}	GGA	—	—	—	464.40	—	—	3.961	2.268	5.396	3.948	0.035
	Ref.[a]	—	—	—	464.81	—	—	4.62	2.63	6.30	3.78	0.032
Sc^{2+}	GGA	—	—	0.014	402.10	7.274	4.523	2.909	1.650	4.124	3.171	0.020
	Ref.[b,c]	—	—	0.010								
Ti^{2+}	GGA	7.784	4.827	0.020	457.28	8.279	5.143	3.384	1.923	4.725	3.917	0.028
	Ref.[b,c,d]	6.644	4.107	0.015		9.214	5.744	3.378	1.917	4.850	3.776	0.032
V^{2+}	GGA	8.560	5.304	0.027	515.76	9.112	5.654	3.768	2.149	5.259	4.792	0.036
	Ref.[b,c,d]	7.132	4.460	0.021		9.876	6.153	3.795	2.155	5.352	4.650	0.031
Mn^{4+}	LDA	10.928	6.857	0.060	648.22	11.083	6.960	5.291	3.031	7.086	7.011	0.071
	GGA	10.931	6.859	0.059	648.86	11.086	6.962	5.241	3.002	7.045	7.022	0.070
	Hybrid	10.852	6.807	0.058	659.02	11.005	6.908	5.153	2.952	6.956	7.074	0.070
	Ref.[c,d]					13.177	8.299	5.776	3.288	7.658	6.845	0.066
Cr^{2+}	GGA	8.970	5.561	0.035	577.77	9.327	5.792	3.931	2.248	5.537	5.840	0.044
	Ref.[b,c,e]	8.020	5.359	0.029		10.522	6.552	4.024	2.388	5.841	5.668	0.041
Mn^{3+}	LDA	10.755	6.718	0.053	644.79	11.088	6.933	4.887	2.798	6.698	7.016	0.063
	GGA	10.749	6.715	0.052	645.44	11.085	6.932	4.839	2.770	6.657	7.027	0.063
	Hybrid	10.646	6.647	0.052	655.15	10.996	6.873	4.766	2.728	6.579	7.079	0.063
	Ref.[b,c,d]	10.116	5.741	0.044		12.201	7.649	5.179	3.288	6.988	6.845	0.066
Mn^{2+}	LDA	10.000	6.197	0.046	642.32	10.652	6.614	4.464	2.555	6.226	7.020	0.056
	GGA	9.997	6.197	0.045	642.97	10.648	6.613	4.417	2.527	6.186	7.029	0.056
	Hybrid	9.880	6.120	0.046	652.28	10.561	6.556	4.359	2.494	6.120	7.082	0.057
	Ref.[b,c,d]	8.719	5.195	0.043		11.155	6.943	4.606	2.618	6.321	6.846	0.053
Fe^{2+}	GGA	10.615	6.572	0.061	710.82	11.231	6.9608	5.018	2.864	6.761	8.408	0.075
	Ref.[b,c,d]	9.814	6.095	0.051		11.779	7.327	5.004	2.844	6.793	8.200	0.067
Co^{2+}	GGA	11.255	6.967	0.077	782.33	11.880	7.361	5.424	3.096	7.236	9.955	0.093
	Ref.[b,c,e]	10.564	6.821	0.066		12.396	7.708	5.397	3.069	7.260	9.748	0.092
Ni^{2+}	GGA	11.560	7.154	0.095	857.19	12.021	7.446	5.684	3.245	7.541	11.689	0.113
	Ref.[b,c,e]	10.779	7.548	0.081				5.787	3.291	7.721	11.507	0.102
Cu^{2+}	GGA	—	—	0.116	935.52	—	—	—	—	—	13.668	—
	Ref.[b,c]	—	—	0.103		—	—	—	—	—		—

[a] In the ES columns, the reference values were taken from ref. 49. [b] In the GS columns, the reference values were taken from ref. 52. [c] Some sections were left blank because we have not found relevant data. [d] In the ES columns, the reference values were taken from ref. 50. [e] In the ES columns, the reference values were taken from ref. 51.

at the scalar ZORA relativistic level of theory employing DFT functional parameterization using the LDA, GGA and hybrid formalisms. But only the results obtained with the GGA functional are shown in Fig. 1, for clarity. The Mn atom is represented with STO basis sets, in which the 3d orbitals are expanded with respect to three STO functions with screening constants of 5.95, 2.85 and 1.32.[47] These three STO primitives are also graphically represented in Fig. 1. The influence of the degree of oxidation of the Mn ion on R_{3d} is reflected by the contraction of the tails of the radial functions toward zero (the position of the nucleus), in line with previous theoretical observations.[48] Besides, R_{3d} also becomes sharper upon modifying the electron configuration from $3d^n$ to $2p^5 3d^{n+1}$ (Fig. 1), due to the presence of 2p core-hole in the Mn ions.

Table 1 lists the calculated Slater–Condon integrals corresponding to the $3d^n$ and $2p^5 3d^{n+1}$ electron configurations for Mn^{2+}, Mn^{3+} and Mn^{4+} as well as selective transition metal ions. In the series Mn^{2+}, Mn^{3+} and Mn^{4+}, the parameters increase as the radial functions shrink (see Fig. 1). The LFDFT parameters are not impacted by the changes in the DFT functional along the calculations (Table 1). In the $3d^n$ configuration, the mean deviation between the calculated and experimental deduced Slater–Condon integrals is relatively small (Table 1), showing good estimation of the experiments by DFT. In the $2p^5 3d^{n+1}$ configurations, the agreement between the calculated and reference Slater–Condon integrals is also good (Table 1). Note however that the reference values for $2p^5 3d^{n+1}$ are not based on the fit to experiments but rather the results of scaled-down theoretical values from Hartree–Fock calculations.[42,49–51] The scaling factors range from about 80% or 85% reduction of the Hartree–Fock values, as often reported in the literature.[49–51] The results of the calculation of the spin–orbit coupling constants do strongly depend upon the level of approximation chosen: *i.e.* the Pauli relativistic approach (eqn (11)) *versus* the ZORA spin–orbit method (eqn (14), *vide infra*). Fig. 2 shows the calculated ζ_{3d} and ζ_{2p} values for transition metal ions in the series Ca^{2+}, Sr^{2+}, Ti^{2+}… and Cu^{2+}. They are compared with existing experimental data.[49,50–52] Using the radial functions R_{2p} and R_{3d} in eqn (11), the parameters are overestimated if compared to the experiments as general trends in the transition metal series (Fig. 2). On average, this overestimation is accompanied by factors of 1.75 and 1.10 *vis-à-vis* the experimental data (see Fig. 2) for the 3d and 2p electrons, respectively. The spin–orbit coupling constants can alternatively be calculated using the ZORA spin–orbit method. This is the second calculation route pointed out in the Methodology section. The ZORA Hamiltonian is shown in eqn (13). It results from the zeroth-order regular expansion in $\varepsilon/(2c^2 - V)$ of the Dirac equation[53] which in general gives very accurate results in atomic calculations, *i.e.* eigenfunctions and eigenvalues of core and valence orbitals.[54,55] The expression in eqn (13) is implemented in the ADF program package[26–28] and already combines the operator terms dedicated to both scalar relativistic and spin–orbit coupling.[53,54]

$$\left(-V + \sigma.\mathbf{p}\frac{c^2}{2c^2 - V}\sigma.\mathbf{p}\right)\Phi^{\mathrm{ZORA}} = \varepsilon^{\mathrm{ZORA}}\Phi^{\mathrm{ZORA}} \qquad (13)$$

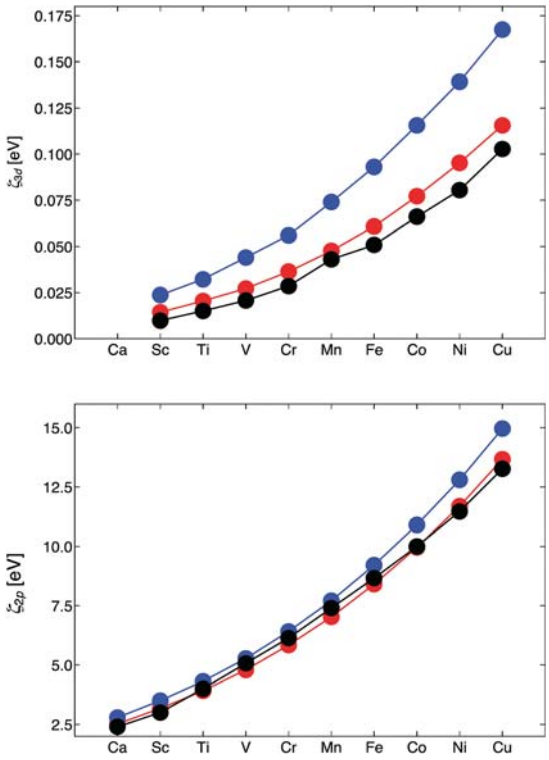

Fig. 2 Calculated spin–orbit coupling constants ζ_{3d} (up) and ζ_{2p} (down) in the series Ca^{2+}, Sc^{2+}, … and Cu^{2+}, obtained using the radial functions R_{nl} (in blue) and ZORA spin–orbit relativistic method (in red), together with available experimental data (in black).

The spin–orbit coupling constants for any open-shell electrons can be determined using the following relationship:

$$\zeta_{nl}^{\mathrm{ZORA}} = \frac{2}{2l+1}\left(\varepsilon_{nl,j=l+\frac{1}{2}}^{\mathrm{ZORA}} - \varepsilon_{nl,j=l-\frac{1}{2}}^{\mathrm{ZORA}}\right) \qquad (14)$$

where, $\varepsilon_{nl,j=l+1/2}$ and $\varepsilon_{nl,j=l-1/2}$ are eigenvalues of eqn (13) belonging especially to the atomic orbitals with a dominant *nl* character, for instance 2p and 3d.

Fig. 2 shows the spin–orbit coupling constants (ζ_{3d} and ζ_{2p}) obtained by means of the ZORA spin–orbit method (eqn (14)) for the series of divalent transition metal ions. The parameters are also listed in Table 1. It is seen that the deviation of the parameters *vis-à-vis* the experiments is clearly smaller for both 3d and 2p electrons (Fig. 2). Note that in the actual version of the LFDFT program in ADF,[26–28] the spin–orbit coupling constants are still calculated by eqn (11). A newer version using eqn (14) is under construction, but one can manually scale down the parameters with correction factors. These correction factors in principle take values in between 0 and 1 and allow decreasing the magnitude of the overestimated spin–orbit coupling interaction in LFDFT. They have to be specified in the input of the calculation with motivation that they will not impinge into the ultimate goal of the LFDFT approach, *i.e.* a non-empirical ligand-field calculation. Thus, the correction factors are the ratio between the parameters calculated from eqn (14) to the solution obtained from eqn (11). For systems with divalent transition metal ions, our results indicate that the

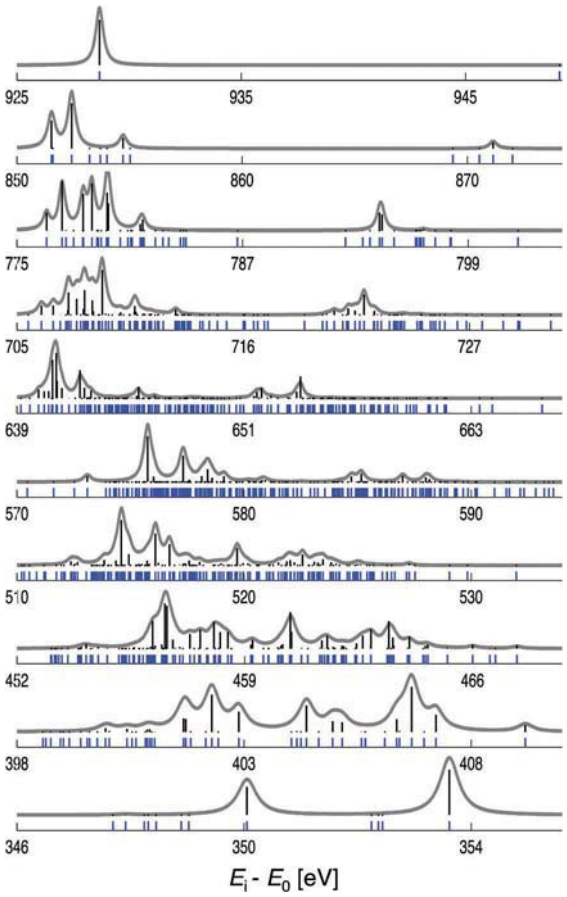

Fig. 3 LFDFT multiplet energy levels of the $2p^53d^{n+1}$ electron configuration (in blue) and oscillator strengths of the electric-dipole allowed $3d^n \rightarrow 2p^53d^{n+1}$ transitions (in black) for Ca^{2+}, Sr^{2+}, Ti^{2+}, V^{2+}, Cr^{2+}, Mn^{2+}, Fe^{2+}, Co^{2+}, Ni^{2+} and Cu^{2+}, with n = 0, 1, 2, 3, 4, 5, 6, 7, 8 and 9, respectively (from bottom to top). The grey curve represents the Lorentzian convolution of the oscillator strengths with γ_i = 0.2 eV. In the ordinate, the intensity plot is given in arbitrary units. The LFDFT parameters are listed in Table 1.

correction factors are in average 0.65 and 0.91 for the 3d and 2p electrons, respectively.

Fig. 3 shows the LFDFT results of the multiplet energy levels of the $2p^53d^{n+1}$ electron configurations together with the calculated intensity of the $3d^n \rightarrow 2p^53d^{n+1}$ transitions for metal ions in the series Ca^{2+}, Sr^{2+}, Ti^{2+},... and Cu^{2+}. The multiplet levels are listed in Table 2, with respect to Russel-Saunders coupling and spin–orbit coupling schemes together with the dimension of the effective ligand-field Hamiltonian calculated by means of eqn (7) and (8). The intensity calculations are obtained within the electric-dipolar approximation. They are normalized to one, in order to facilitate the comparison between different electron configuration systems.

$$I = \sum_{i=1}^{N\left(2p^53d^{n+1}\right)} \left|\left\langle 2p^53d^{n+1}, \Gamma_i \middle| \mathbf{r} \middle| 3d^n, \Gamma_0 \right\rangle\right|^2 \frac{\gamma_i}{\pi((h\nu + E_0 - E_i) + \gamma_i^2)} \quad (15)$$

In the right-hand side of eqn (15), the first term designates the oscillator strength calculation (*i.e.* transition probability) of the $3d^n(\Gamma_0) \rightarrow 2p^53d^{n+1}(\Gamma_i)$ transition in the electric-dipolar approximation. In Fig. 3, it is illustrated by bar diagrams placed above the representation of the multiplet energy levels. The term $|3d^n, \Gamma_0\rangle$ refers to the ground state of the $3d^n$ electron configuration (see Table 2) with E_0 as the LFDFT eigenvalue. The term $|2p^53d^{n+1}, \Gamma_i\rangle$ refers to the whole manifold of the multiplet states of the $2p^53d^{n+1}$ electron configurations (see Table 2) with E_i as LFDFT eigenvalues. The term **r** stands for the electric-dipole moment operator, which is expanded in terms of spherical harmonics of order l = 1. The second term in eqn (15) represents a Lorentzian function, which is used for the broadening of the oscillator strengths to account for intrinsic effects related to the finite lifetime of the core-hole $|2p^53d^{n+1}, \Gamma_i\rangle$ states and, to a lesser extent, to the finite experimental resolution. It is also graphically represented in Fig. 3. The term $h\nu$ represents the energy of the absorbed photon; and the parameter γ_i is the half-width at half-maximum of the Lorentzian function (eqn (15)). A comparative view of the intensity plot for Mn^{2+}, Mn^{3+} and Mn^{4+} ions is available in the ESI,† Fig. S1.

Note that the parameter γ_i (eqn (15)) is not deduced from theoretical calculations in LFDFT but rather imposed by educated guess.[56] In Fig. 3, the oscillator strengths are convoluted with the Lorentzian function with a constant value for the half-width at half-maximum parameter (*i.e.* $\gamma_i = \gamma$ = 0.20 eV). It is observed that only atomic spectral terms ($|2p^53d^{n+1}, \Gamma_i\rangle$) assimilated with ΔJ = 0, ± 1 *vis-à-vis* $|3d^n, \Gamma_0\rangle$ possess non-zero transition probabilities fulfilling the electric-dipole moment selection rules, with exception for Ca^{2+} and Cr^{2+} where the selection rule ΔJ = 0 does not hold. Since the values of the spin–orbit coupling constants dedicated to the 2p electrons are particularly large (Table 1) for systems with the $2p^53d^{n+1}$ configurations, the multiplet levels in Fig. 3 are mainly composed of final states with different representations in Table 2. For example in Ca^{2+} ions (Fig. 3), the three atomic multiplets with non-zero transition probabilities originate from a linear combination of final states with $^1P_1$, $^3D_1$ and $^3P_1$ representations belonging to the $2p^53d^1$ configuration (see Table 2). For the atomic multiplet with the highest intensity, the fractional parentages are 61.15%, 32.67% and 6.18%, respectively, for $^1P_1$, $^3D_1$ and $^3P_1$. Note also that we obtain a relatively large Δ value in the LFDFT calculations employing the hybrid functional (Table 1), which in the present work leads to a red shift in the energy scale of the multiplet energy levels (see also the ESI,† Fig. S2). The overestimation of this parameter may originate from misrepresentation of the exchange potential at long-range interactions, which is often reported in the literature to induce errors for excitation energies to Rydberg excited states.[57,58] However, we must point out that hybrid functionals are often valuable in calculations involving the TDDFT model of core-electron excitation.[59]

The impacts of the ligand-field splitting interaction (eqn (12)) are illustrated with two examples for applications: $SrTiO_3$ and MnF_2. The motivation of these examples is the local atomic environments of the transition metal ions, which possess a regular and a distorted octahedron for $SrTiO_3$ and MnF_2, respectively. Furthermore, Ti and Mn $L_{2,3}$-edge X-ray absorption spectra are available for comparison and validation of the

Table 2 Spectral terms notation of the atomic multiplet structure (Γ) arising from the $3d^n$ and $2p^5 3d^{n+1}$ electron configurations (Config.) representing the ground (GS) and excited (ES) states of transition metal ions, with n = 0, 1, 2, ... and 9, under investigation in this work. N stands for the total number of single determinants belonging to the electron configuration system

	GS			ES		
n	Config.	N^a	$\Gamma^{b,c}$	Config.	N^a	Γ^b
0	$3d^0$	1	$[^1S_0]$	$2p^5 3d^1$	60	$^1P_1$, $^1D_2$, $^1F_3$, $^3P_{0,1,2}$, $^3D_{1,2,3}$ and $^3F_{2,3,4}$
1	$3d^1$	10	$^2D_{[3/2],5/2}$	$2p^5 3d^2$	270	$3 \times {}^2P_{1/2,3/2}$, $3 \times {}^2D_{3/2,5/2}$, $3 \times {}^2F_{5/2,7/2}$, $2 \times {}^2G_{7/2,9/2}$, $^2H_{9/2,11/2}$, $^4S_{3/2}$, $^4P_{1/2,3/2,5/2}$, $2 \times {}^4D_{1/2,3/2,5/2,7/2}$, $^4F_{3/2,5/2,7/2,9/2}$ and $^4G_{5/2,7/2,9/2,11/2}$
2	$3d^2$	45	$^1S_0$, $^1D_2$, $^1G_4$, $^3P_{0,1,2}$ and $^3F_{[2],3,4}$	$2p^5 3d^3$	720	$^1S_0$, $3 \times {}^1P_1$, $4 \times {}^1D_2$, $4 \times {}^1F_3$, $3 \times {}^1G_4$, $2 \times {}^1H_5$, $^1I_6$, $2 \times {}^3S_1$, $4 \times {}^3P_{0,1,2}$, $6 \times {}^3D_{1,2,3}$, $5 \times {}^3F_{2,3,4}$, $4 \times {}^3G_{3,4,5}$, $2 \times {}^3H_{4,5,6}$, $^3I_{5,6,7}$ $^5S_2$, $^5P_{1,2,3}$, $2 \times {}^5D_{0,1,2,3,4}$, $^5F_{1,2,3,4,5}$ and $^5G_{2,3,4,5,6}$
3	$3d^3$	120	$^2P_{1/2,3/2}$, $2 \times {}^2D_{3/2,5/2}$, $^2F_{5/2,7/2}$, $^2G_{7/2,9/2}$, $^2H_{9/2,11/2}$, $^4P_{1/2,3/2,5/2}$ and $^4F_{[3/2],5/2,7/2,9/2}$	$2p^5 3d^4$	1260	$2 \times {}^2S_{1/2}$, $7 \times {}^2P_{1/2,3/2}$, $8 \times {}^2D_{3/2,5/2}$, $9 \times {}^2F_{5/2,7/2}$, $7 \times {}^2G_{7/2,9/2}$, $5 \times {}^2H_{9/2,11/2}$, $2 \times {}^2I_{11/2,13/2}$, $^2K_{13/2,15/2}$, $2 \times {}^4S_{3/2}$, $4 \times {}^4P_{1/2,3/2,5/2}$, $6 \times {}^4D_{1/2,3/2,5/2,7/2}$, $5 \times {}^4F_{3/2,5/2,7/2,9/2}$, $4 \times {}^4G_{5/2,7/2,9/2,11/2}$, $2 \times {}^4H_{7/2,9/2,11/2,13/2}$, $^4I_{9/2,11/2,13/2,15/2}$, $^6P_{3/2,5/2,7/2}$, $^6D_{1/2,3/2,5/2,7/2,9/2}$ and $^6F_{1/2,3/2,5/2,7/2,9/2,11/2}$
4	$3d^4$	210	$2 \times {}^1S_0$, $2 \times {}^1D_2$, $^1F_3$, $^1I_6$, $2 \times {}^1G_4$, $2 \times {}^3P_{0,1,2}$, $^3D_{1,2,3}$, $2 \times {}^3F_{2,3,4}$, $^3G_{3,4,5}$, $^3H_{4,5,6}$ and $^5D_{[0],1,2,3,4}$	$2p^5 3d^5$	1512	$^1S_0$, $5 \times {}^1P_1$, $6 \times {}^1D_2$, $7 \times {}^1F_3$, $5 \times {}^1G_4$, $4 \times {}^1H_5$, $2 \times {}^1I_6$, $^1K_7$, $2 \times {}^3S_1$, $7 \times {}^3P_{0,1,2}$, $9 \times {}^3D_{1,2,3}$, $10 \times {}^3F_{2,3,4}$, $7 \times {}^3G_{3,4,5}$, $5 \times {}^3H_{4,5,6}$, $2 \times {}^3I_{5,6,7}$, $^3K_{6,7,8}$, $^5S_2$, $3 \times {}^5P_{1,2,3}$, $3 \times {}^5D_{0,1,2,3,4}$, $3 \times {}^5F_{1,2,3,4,5}$, $2 \times {}^5G_{2,3,4,5,6}$, $^5H_{3,4,5,6,7}$ and $^7P_{2,3,4}$
5	$3d^5$	252	$^2S_{1/2}$, $^2P_{1/2,3/2}$, $3 \times {}^2D_{3/2,5/2}$, $2 \times {}^2F_{5/2,7/2}$, $2 \times {}^2G_{7/2,9/2}$, $^2H_{9/2,11/2}$, $^2I_{11/2,13/2}$, $^4P_{1/2,3/2,5/2}$, $^4D_{1/2,3/2,5/2,7/2}$, $^4F_{3/2,5/2,7/2,9/2}$, $^4G_{5/2,7/2,9/2,11/2}$ and $[^6S_{5/2}]$	$2p^5 3d^6$	1260	$2 \times {}^2S_{1/2}$, $7 \times {}^2P_{1/2,3/2}$, $8 \times {}^2D_{3/2,5/2}$, $9 \times {}^2F_{5/2,7/2}$, $7 \times {}^2G_{7/2,9/2}$, $5 \times {}^2H_{9/2,11/2}$, $2 \times {}^2I_{11/2,13/2}$, $^2K_{13/2,15/2}$, $2 \times {}^4S_{3/2}$, $4 \times {}^4P_{1/2,3/2,5/2}$, $6 \times {}^4D_{1/2,3/2,5/2,7/2}$, $5 \times {}^4F_{3/2,5/2,7/2,9/2}$, $4 \times {}^4G_{5/2,7/2,9/2,11/2}$, $2 \times {}^4H_{7/2,9/2,11/2,13/2}$, $^4I_{9/2,11/2,13/2,15/2}$, $^6P_{3/2,5/2,7/2}$, $^6D_{1/2,3/2,5/2,7/2,9/2}$ and $^6F_{1/2,3/2,5/2,7/2,9/2,11/2}$
6	$3d^6$	210	$2 \times {}^1S_0$, $2 \times {}^1D_2$, $^1F_3$, $^1I_6$, $2 \times {}^1G_4$, $2 \times {}^3P_{0,1,2}$, $^3D_{1,2,3}$, $2 \times {}^3F_{2,3,4}$, $^3G_{3,4,5}$, $^3H_{4,5,6}$ and $^5D_{0,1,2,3,[4]}$	$2p^5 3d^7$	720	$^1S_0$, $3 \times {}^1P_1$, $4 \times {}^1D_2$, $4 \times {}^1F_3$, $3 \times {}^1G_4$, $2 \times {}^1H_5$, $^1I_6$, $2 \times {}^3S_1$, $4 \times {}^3P_{0,1,2}$, $6 \times {}^3D_{1,2,3}$, $5 \times {}^3F_{2,3,4}$, $4 \times {}^3G_{3,4,5}$, $2 \times {}^3H_{4,5,6}$, $^3I_{5,6,7}$ $^5S_2$, $^5P_{1,2,3}$, $2 \times {}^5D_{0,1,2,3,4}$, $^5F_{1,2,3,4,5}$ and $^5G_{2,3,4,5,6}$
7	$3d^7$	120	$^2P_{1/2,3/2}$, $2 \times {}^2D_{3/2,5/2}$, $^2F_{5/2,7/2}$, $^2G_{7/2,9/2}$, $^2H_{9/2,11/2}$, $^4P_{1/2,3/2,5/2}$ and $^4F_{3/2,5/2,7/2,[9/2]}$	$2p^5 3d^8$	270	$3 \times {}^2P_{1/2,3/2}$, $3 \times {}^2D_{3/2,5/2}$, $3 \times {}^2F_{5/2,7/2}$, $2 \times {}^2G_{7/2,9/2}$, $^2H_{9/2,11/2}$, $^4S_{3/2}$, $^4P_{1/2,3/2,5/2}$, $2 \times {}^4D_{1/2,3/2,5/2,7/2}$, $^4F_{3/2,5/2,7/2,9/2}$ and $^4G_{5/2,7/2,9/2,11/2}$
8	$3d^8$	45	$^1S_0$, $^1D_2$, $^1G_4$, $^3P_{0,1,2}$ and $^3F_{2,3,[4]}$	$2p^5 3d^9$	60	$^1P_1$, $^1D_2$, $^1F_3$, $^3P_{0,1,2}$, $^3D_{1,2,3}$ and $^3F_{2,3,4}$
9	$3d^9$	10	$^2D_{3/2,[5/2]}$	$2p^5 3d^{10}$	6	$^2P_{1/2,3/2}$

[a] The values of N are determined by means of eqn (7) and (8) for GS and ES, respectively. [b] For all entries in Table 1, the notation of multiplets uses the quantum S, L and J numbers (*i.e.* $^{2S+1}L_J$) and the number in front of the multiplets (*e.g.* $2 \times {}^1S_0$) denotes the multiple occurrence of the term $^1S_0$ in this electron configuration system. [c] The ground states of the $3d^n$ configuration are put in square brackets.

theoretical results.[60,61] $SrTiO_3$ crystallizes in the cubic perovskite structure type.[62] The Ti^{4+} ion is surrounded by six O^{2-} ligands with O_h symmetry. The DFT calculation is performed on the molecular $(TiO_6)^{8-}$ cluster with a Ti–O bond length of 1.950 Å, in line with the experimental data.[62] An external electrostatic potential is also introduced *via* a set of point charges, which allow simulation of the Madelung potential representing the long-range interaction due to the periodicity of the $SrTiO_3$ crystal structure. Namely, we use point charges located in the lattice positions of Sr (with Q = +2), Ti (with Q = +4) and O (with Q = −2) around the molecular $(TiO_6)^{8-}$ cluster. MnF_2 crystallizes in a distorted rutile structure type,[62,63] where the Mn^{2+} center is surrounded by six F^- ligands with C_{2h} coordination. The deviation of the structure from ideal O_h symmetry is due to tetragonal plus rhombic distortions. The tetragonal distortion is responsible for the appearance of two non-equivalent bond lengths: d_e and d_a, which are formed by Mn^{2+} with the four equatorial and two axial F^- ligands, respectively. The rhombic distortion implies $\theta \neq 90^\circ$, which is the bond angle formed by F–Mn–F in the equatorial plane. The DFT run is performed on the molecular $(MnF_6)^{4-}$ cluster with d_e = 2.131 Å, d_a = 2.104 Å and $\theta = 78^\circ$, in line with the experimental data.[63,64] An external electrostatic potential is also introduced using a similar procedure to that described earlier for $SrTiO_3$.

In $(TiO_6)^{8-}$, the fivefold 3d orbitals of Ti^{4+} split into three lower energy and two upper energy molecular orbitals, usually designated as t_{2g}^* (with dominant $3d_{xy}$, $3d_{xz}$, $3d_{yz}$ characters) and e_g^* (with dominant $3d_{z^2}$, $3d_{x^2-y^2}$ characters), respectively, which are shown in the molecular orbitals diagram in Fig. 4. The threefold 2p orbitals remain degenerate and belong to t_{1u} irreps. The ligand field potential in eqn (12) is parameterized by only B_0^4(3d,3d) and B_4^4(3d,3d). The term B_q^k(2p,3d) in eqn (12) vanishes because of the inversion center in the O_h point group, which ensures forbidden mixtures between functions assimilated with opposite parity.[65,66] In $(MnF_6)^{4-}$, the degeneracy of 3d is completely lifted in C_{2h}. But the energy splitting resembles the O_h pattern, since we obtain three molecular orbitals with lower energy (see Fig. 4): a_g^* (with dominant $3d_{xy}$ character), b_g^* ($3d_{yz}$) and b_g^* ($3d_{xz}$) and two molecular orbitals with higher energy: a_g^* (with dominant $3d_{z^2}$ character) and a_g^* ($3d_{x^2-y^2}$). The degeneracy of the 2p orbitals is also lifted in C_{2h}, obtaining three distinct molecular orbitals: a_u (with dominant $2p_z$ character), b_u ($2p_y$) and b_u ($2p_x$). The calculated parameters for the ligand-field potential for $(TiO_6)^{8-}$ and $(MnF_6)^{4-}$ are listed in Table 3, which are in agreement with the reported values in the literature.[40,51,67] They are obtained from DFT calculations employing the GGA functional. Note that the resulting energy splitting of the 2p orbitals in $(MnF_6)^{4-}$ is relatively small, in the magnitude of 10^{-3} eV. Note also that, the

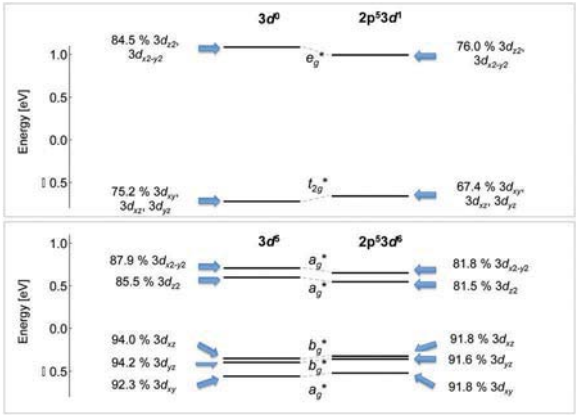

Fig. 4 Energies of the molecular orbitals with dominant 3d characters of Ti^{4+} (up) and Mn^{2+} (down) in $(TiO_6)^{8-}$ and $(MnF_6)^{4-}$, calculated for the $3d^n$ and $2p^53d^{n+1}$ configurations, with n = 0 and 5, respectively. Note that in LFDFT, the trace of the ligand-field potential is zero (*i.e.* $B_0^0(3d,3d) = 0$).

elongation and compression of the Ti–O or Mn–F bond lengths are the factors that influence the parameters, as tested in our work.

The molecular orbitals with dominant 2p and 3d characters of Ti^{4+} and Mn^{2+} (see Fig. 4) are associated with radial functions with different shapes. This depends on the interaction (bonding regime and covalency) of each component of 2p and 3d with the ligand orbitals. This is illustrated in Fig. 5 for the 3d orbitals of Ti^{4+}. The two radial functions with different shapes, namely R_{3d,e_g} and $R_{3d,t_{2g}}$ (Fig. 5), are attributed to the splitting of the 3d orbitals into t_{2g}* and e_g* under the effect of the O_h ligand-field in the $2p^53d^1$ configuration. A similar situation occurs for Mn^{2+} ions in $(MnF_6)^{4-}$, which can be seen in the ESI,† Fig. S3. The phenomenology of the nephelauxetic effect of Jørgensen[69,70] is reflected in Fig. 5 and Fig. S3 (ESI†). In particular, the shape of R_{3d} varies from a free ion to a molecular cluster because of the expansion of the electron clouds towards the positions of the ligands. The nephelauxetic effect denotes the reduction of the values of the inter-electronic repulsion and spin–orbit coupling parameters obtained for the molecular cluster if compared to the free ion. However, within the ligand-field scheme, there is no *ml* dependency for the atomic basis functions. That is, the electrons are supposed to move in a central field. Thus, we construct artificial radial functions, which complies with the fundamental concept of ligand-field theory,[16–19] as follows:

$$R_{nl,\mathrm{av}} = \frac{1}{2l+1}\sum_{i}^{2l+1} R_{nl,i} \qquad (16)$$

where, $R_{nl,i}$ is the radial function obtained for the component i of the Kohn–Sham orbitals with a dominant nl character, expanded in terms of STO functions[47] or projected on a numerical grid;[68] $R_{nl,\mathrm{av}}$ is the artificial radial function from which the Slater–Condon parameters are calculated using eqn (3)–(5).

For the 3d orbitals of Ti^{4+}, $R_{3d,\mathrm{av}}$ is also graphically represented in Fig. 5. The calculated Slater–Condon integrals are listed in Table 3 for systems with $(TiO_6)^{8-}$ and $(MnF_6)^{4-}$, obtained from DFT calculation employing the GGA functional and the ZORA

Table 3 LFDFT parameters (in eV) for systems with $(TiO_6)^{8-}$ and $(MnF_6)^{4-}$ having $3d^n$ (GS) and $2p^53d^{n+1}$ (ES) configurations of Ti^{4+} and Mn^{2+}, with n = 0 and 5, respectively, obtained from DFT calculations using the GGA functional. The parameter β (in [—]) represents the nephelauxetic ratio

	$(TiO_6)^{8-}$		$(MnF_6)^{4-}$	
	GGA	β	GGA	β
GS				
$F^2(3d,3d)$	0	—	8.404	0.841
$F^4(3d,3d)$	0	—	5.176	0.835
ζ_{3d}	0	—	0.041	0.911
$B_0^4(3d,3d)$	0	—	2.140	—
$B_1^4(3d,3d)$	0	—	0	—
$B_2^4(3d,3d)$	0	—	0.257i	—
$B_3^4(3d,3d)$	0	—	0	—
$B_4^4(3d,3d)$	0	—	1.418	—
$B_0^2(3d,3d)$	0	—	0.323	—
$B_1^2(3d,3d)$	0	—	0	—
$B_2^2(3d,3d)$	0	—	0.390i	—
ES				
$F^2(3d,3d)$	0	—	8.233	0.773
$F^4(3d,3d)$	0	—	5.084	0.769
$G^1(2p,3d)$	2.986	0.754	3.813	0.863
$G^3(2p,3d)$	1.707	0.753	2.181	0.863
$F^2(2p,3d)$	4.286	0.794	5.346	0.864
ζ_{2p}	3.915	0.992	7.027	1.000
ζ_{3d}	0.027	0.771	0.048	0.857
Δ	460.11	0.991	642.63	1.000
$B_0^2(2p,2p)$	0	—	0.023	—
$B_1^2(2p,2p)$	0	—	0	—
$B_2^2(2p,2p)$	0	—	0.020i	—
$B_0^4(3d,3d)$	3.473	—	1.963	—
$B_1^4(3d,3d)$	0	—	0	—
$B_2^4(3d,3d)$	0	—	0.222i	—
$B_3^4(3d,3d)$	0	—	0	—
$B_4^4(3d,3d)$	2.076	—	1.314	—
$B_0^2(3d,3d)$	0	—	0.325	—
$B_1^2(3d,3d)$	0	—	0	—
$B_2^2(3d,3d)$	0	—	0.322i	—

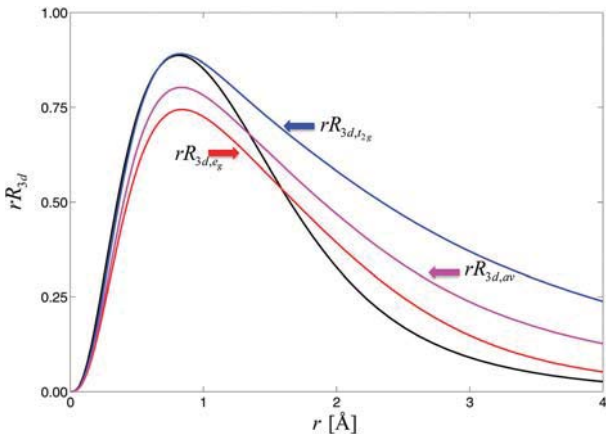

Fig. 5 Radial functions of the Kohn–Sham orbitals with dominant 3d character of Ti^{4+} obtained for the $2p^53d^1$ electron configuration in the free ion (in black) and in $(TiO_6)^{8-}$ embedded in $SrTiO_3$ (in red and blue). The magenta curve represents the artificial 3d radial function used in the LFDFT calculation (see the text for details).

scalar relativistic method. The calculated spin–orbit coupling constants are also listed in Table 3. The parameters are obtained for the ground $3d^0$ and $3d^5$, configurations of the Ti^{4+} and Mn^{2+} ions, respectively, as well as the excited $2p^53d^1$ and $2p^53d^6$. The reduction of the parameters *vis-à-vis* the free ion is expressed by the constant β of Jørgensen,[69] which is calculated and listed in Table 3 for Ti^{4+} and Mn^{2+} in the molecular $(TiO_6)^{8-}$ and $(MnF_6)^{4-}$ cluster systems.

Fig. 6 and 7 show the calculated multiplet energy levels corresponding to the $2p^53d^1$ and $2p^53d^6$ electron configurations of Ti^{4+} and Mn^{2+} in the systems $(TiO_6)^{8-}$ and $(MnF_6)^{4-}$, respectively. The simulated absorption spectra of the 2p core-electron excitation are also shown. The LFDFT calculations are restricted to the $3d^0 \rightarrow 2p^53d^1$ for Ti^{4+} and $3d^5 \rightarrow 2p^53d^6$ transitions for Mn^{2+}. In the intensity calculations (see eqn (15)), the initial state represents the ground states of the $3d^0$ and $3d^5$ configurations of Ti^{4+} and Mn^{2+} in the respective molecular cluster. On the other hand, the final states are composed of the whole manifold of the multiplet structure of the $2p^53d^1$ for Ti^{4+} (see Fig. 6) and $2p^53d^6$ transitions for Mn^{2+} (see Fig. 7).

The Ti^{4+} ion has a non-degenerate multiplet ground state because of the $3d^0$ configuration. That is, the ground state is $^1S_0$ (see Table 2), *i.e.* Γ_1 in Bethe notation, taking into account the octahedral ligand-field splitting. In the $2p^53d^1$ configuration, with inclusion of the octahedral ligand-field splitting, the atomic multiplet terms assimilated with $J = 0$ (Table 2) is transformed into the Γ_1 irreps of the O* double group.

Similarly, the atomic multiplet terms with $J = 1$ (see Table 2) is transformed into Γ_4; $J = 2$ to Γ_3 and Γ_5; $J = 3$ to Γ_2, Γ_4 and Γ_5; $J = 4$ to Γ_1, Γ_3, Γ_4 and Γ_5. The final states of the 2p core-electron excitation form the basis of the following representations of the O* double group: $2 \times \Gamma_1$, $3 \times \Gamma_2$, $5 \times \Gamma_3$, $7 \times \Gamma_4$ and $8 \times \Gamma_5$. Within the electric-dipolar approximation, Γ_4 only does possess non-zero transition probability, *i.e.* we obtain in total seven multiplet levels with allowed transitions. More particularly, this is illustrated in the calculated absorption spectrum in Fig. 6. Two multiplets have the highest intensities. They lie at energies of 460 eV and 466 eV (see Fig. 6) and they are also visible in the free ion spectrum. Five other multiplets have smaller absorption coefficients and mainly result from the redistribution of the intensity due to the octahedral ligand-field splitting. In the experimental Ti^{4+} $L_{2,3}$-edge X-ray absorption spectrum, the bands observed for $SrTiO_3$[60] are in good agreement with the theoretical results in terms of energies and relative intensities.

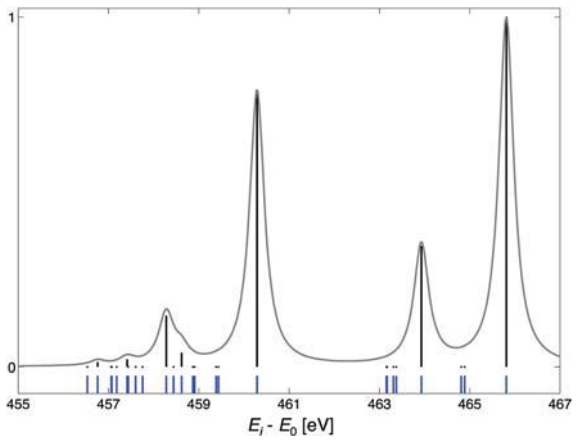

Fig. 6 LFDFT results of the multiplet energy levels (in blue) of the $2p^53d^1$ configuration of Ti^{4+} in the molecular $(TiO_6)^{8-}$ cluster embedded in $SrTiO_3$. The oscillator strengths of the $3d^0 \rightarrow 2p^53d^1$ transitions are shown with bar diagrams placed above the multiplet energies (in black). The grey curves represent the Lorentzian convolution of the oscillator strengths with a half-width at half-maximum γ = 0.2 eV. In the ordinate, the intensity plot is given in arbitrary units.

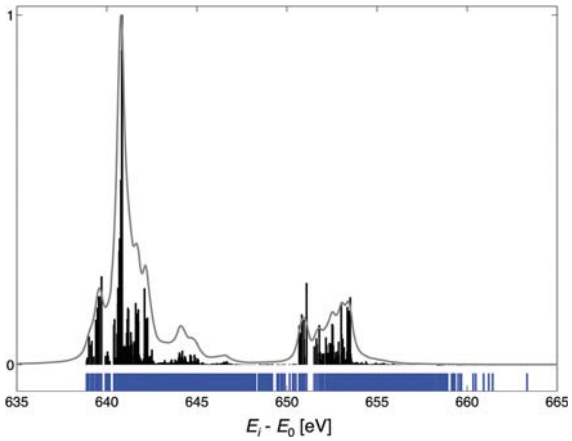

Fig. 7 LFDFT results of the multiplet energy levels (in blue) of the $2p^53d^6$ configuration of Mn^{2+} in the molecular $(MnF_6)^{4-}$ clusters embedded in MnF_2. The oscillator strengths of the $3d^5 \rightarrow 2p^53d^6$ (down) transitions are shown with bar diagrams placed above the multiplet energies (in black). The grey curves represent the Lorentzian convolution of the oscillator strengths with a half-width at half-maximum γ = 0.2 eV. In the ordinate, the intensity plot is given in arbitrary units.

Within the $3d^5$ configuration, the Mn^{2+} ion undergoes a system with 252 × 252 elements in the configuration interaction matrix (see Table 2). The ground state is the high-spin $^6S_{5/2}$, whose energy is split by zero-field splitting into three Kramers doublets with inclusion of the C_{2h} ligand-field splitting in the molecular $(MnF_6)^{4-}$ cluster. The energy separation between these three Kramers doublets is nonetheless very small, in the magnitude of 10^{-5} of eV as a result of our LFDFT calculations. In the $2p^53d^6$ configuration, the atomic mulitplet terms assimilated with J values of 3/2, 5/2 and 7/2 in Table 2 have non-zero transition probabilities, fulfilling the electric-dipole moment selection rules. The difference in the absorption spectra of Mn^{2+} in the free ion and in the molecular cluster is due to the splitting of these atomic multiplet terms into the Kramers doublet belonging all to the Γ_3 representation of the C_2* double group. The calculated absorption spectrum for $(MnF_6)^{4-}$ is also in agreement with the experimental Mn $L_{2,3}$-edge X-ray absorption spectrum of MnF_2.[61]

Conclusions

The purpose of this work was to present methodological advents for the theoretical consideration of the electronic structure and optical properties arising from 2p core-electron excitation in transition metal ions and compounds. In this

context, we have used a theoretical methodology in the LFDFT program, which utilizes the concept from the crystal-/ligand-field model complemented with a first principles DFT calculation. We have calculated the multiplet energy levels arising from the $2p^5 3d^{n+1}$ electron configurations, with n = 0, 1, 2,... and 9, of divalent transition metal ions. The ligand-field parameters such as Slater–Condon integrals, spin–orbit coupling constants and ligand-field potential were determined non-empirically from the DFT calculations. The change of the DFT functional along the LFDFT calculation was analyzed, but the impact of different basis set expansion of the radial functions was not considered. Furthermore, two examples for applications were explicitly treated: $(TiO_6)^{8-}$ and $(MnF_6)^{4-}$, which are selectively cut from the crystal structure of $SrTiO_3$ and MnF_2, respectively. The oscillator strengths of the $3d^n \rightarrow 2p^5 3d^{n+1}$ transitions are also calculated allowing a theoretical simulation of the absorption spectra. A qualitative agreement with respect to the experiment is observed. The energies and intensities of the measured absorption bands are reproduced with details, which are not always visible in the experimental spectral profile, enabling a better understanding of the optical effect induced by the 2p core-electron excitation and a good connection between spectroscopy studies and theoretical investigations in materials science. A newer version of LFDFT in ADF is under preparation, ensuring a more precise calculation of spin–orbit coupling constants.

Acknowledgements

We are grateful to Dr Erik van Lenthe, Dr Stan van Gisbergen and all members of the SCM team in Amsterdam (www.scm.com) for their input and support in installing LFDFT in the ADF program package (ADF2017.103). We also acknowledge the support from the ECOSTBio (COST Action CM1305) and Swissnuclear.

Notes and references

1 M. Atanansov, C. A. Daul and C. Rauzy, *Struct. Bonding*, 2004, **106**, 97.
2 M. Atanasov and C. Daul, *Chimia*, 2005, **59**, 504.
3 M. Atanasov and C. A. Daul, *C. R. Chim.*, 2005, **8**, 1421.
4 M. Atanasov, C. Rauzy, P. Baettig and C. Daul, *Int. J. Quantum Chem.*, 2005, **102**, 119.
5 M. Atanasov, C. A. Daul, M.-M. Rohmer and T. Venkatachalam, *Chem. Phys. Lett.*, 2006, **427**, 449.
6 L. Petit, A. Borel, C. Daul, P. Maldivi and C. Adamo, *Inorg. Chem.*, 2006, **45**, 7382.
7 A. Borel and C. A. Daul, *THEOCHEM*, 2006, **762**, 93.
8 M. Zbiri, C. A. Daul and T. A. Wesolowski, *J. Chem. Theory Comput.*, 2006, **2**, 1106.
9 F. Senn and C. A. Daul, *THEOCHEM*, 2010, **954**, 105.
10 F. Senn, M. Zlatar, M. Gruden-Pavlovic and C. Daul, *Monatsh. Chem.*, 2011, **142**, 593.
11 F. Senn, L. Helm, A. Borel and C. A. Daul, *C. R. Chim.*, 2012, **15**, 250.
12 H. Ramanantoanina, W. Urland, F. Cimpoesu and C. Daul, *Phys. Chem. Chem. Phys.*, 2013, **15**, 13902.
13 H. Ramanantoanina, W. Urland, A. Garcia-Fuente, F. Cimpoesu and C. Daul, *Phys. Chem. Chem. Phys.*, 2014, **16**, 14625.
14 H. Ramanantoanina, M. Sahnoun, A. Barbiero, M. Ferbinteanu and F. Cimpoesu, *Phys. Chem. Chem. Phys.*, 2015, **17**, 18547.
15 H. Ramanantoanina, G. Kuri, C. Daul and J. Bertsch, *Phys. Chem. Chem. Phys.*, 2016, **18**, 19020.
16 H. Bethe, *Ann. Phys.*, 1929, **295**, 133.
17 J. H. van Vleck, *J. Chem. Phys.*, 1935, **3**, 807.
18 C. J. Balhausen, *Introduction to Ligand Field Theory*, McGraw-Hill Co, New York, 1962.
19 B. N. Figgis and M. A. Hitchman, *Ligand Field Theory and Its Applications*, Wiley-VCH, New York, 2000.
20 M. Zbiri, M. Atanasov, C. Daul, J. M. Garcia-Lastra and T. A. Wesolowksi, *Chem. Phys. Lett.*, 2004, **397**, 441.
21 M. Atanasov, C. Daul, H. U. Gudel, T. A. Wesolowski and M. Zbiri, *Inorg. Chem.*, 2005, **44**, 2954.
22 P. Garcia-Fernandez, F. Senn, C. A. Daul, J. A. Aramburu, M. T. Barriuso and M. Moreno, *Phys. Chem. Chem. Phys.*, 2009, **11**, 7545.
23 H. Ramanantoanina, W. Urland, A. Garcia-Fuente, F. Cimpoesu and C. Daul, *Chem. Phys. Lett.*, 2013, **588**, 260.
24 F. Vlahovic, M. Peric, M. Gruden-Pavlovic and M. Zlatar, *J. Chem. Phys.*, 2015, **142**, 214111.
25 H. Ramanantoanina, F. Cimpoesu, C. Göttel, M. Sahnoun, B. Herden, M. Suta, C. Wickleder, W. Urland and C. Daul, *Inorg. Chem.*, 2015, **54**, 8319.
26 G. te Velde, F. M. Bickelhaupt, E. J. Baerends, C. Fonseca-Guerra, S. J. A. van Gisbergen, J. G. Snijders and T. Zigler, *J. Comput. Chem.*, 2001, **22**, 931.
27 C. Fonseca-Guerra, J. G. Snijders, G. te Velde and E. J. Baerends, *Theor. Chem. Acc.*, 1998, **99**, 391.
28 E. J. Baerends, T. Ziegler, A. J. Atkins, J. Autschbach, O. Baseggio, D. Bashford, A. Bérces, F. M. Bickelhaupt, C. Bo, P. M. Boerrigter, L. Cavallo, C. Daul, D. P. Chong, D. V. Chulhai, L. Deng, R. M. Dickson, J. M. Dieterich, D. E. Ellis, M. van Faassen, L. Fan, T. H. Fischer, C. Fonseca Guerra, M. Franchini, A. Ghysels, A. Giammona, S. J. A. van Gisbergen, A. Goez, A. W. Götz, J. A. Groeneveld, O. V. Gritsenko, M. Grüning, S. Gusarov, F. E. Harris, P. van den Hoek, Z. Hu, C. R. Jacob, H. Jacobsen, L. Jensen, L. Joubert, J. W. Kaminski, G. van Kessel, C. König, F. Kootstra, A. Kovalenko, M. V. Krykunov, E. van Lenthe, D. A. McCormack, A. Michalak, M. Mitoraj, S. M. Morton, J. Neugebauer, V. P. Nicu, L. Noodleman, V. P. Osinga, S. Patchkovskii, M. Pavanello, C. A. Peeples, P. H. T. Philipsen, D. Post, C. C. Pye, H. Ramanantoanina, P. Ramos, W. Ravenek, J. I. Rodríguez, P. Ros, R. Rüger, P. R. T. Schipper, D. Schlüns, H. van Schoot, G. Schreckenbach, J. S. Seldenthuis, M. Seth, J. G. Snijders, M. Solà, M. Stener, M. Swart, D. Swerhone, V. Tognetti, G. te Velde, P. Vernooijs, L. Versluis, L. Visscher, O. Visser, F. Wang, T. A. Wesolowski, E. M. van Wezenbeek, G. Wiesenekker, S. K. Wolff, T. K. Woo and A. L. Yakovlev, *ADF2017*, 2017, available at htttp://www.scm.com.
29 F. de Groot, *Chem. Rev.*, 2001, **101**, 1779.
30 P. Glatzel and U. Bergmann, *Coord. Chem. Rev.*, 2005, **249**, 65.

31 R. K. Hocking, E. C. Wasinger, F. M. F. de Groot, K. O. Hodgson, B. Hedman and E. I. Solomon, *J. Am. Chem. Soc.*, 2006, **128**, 10442.
32 W. G. Waddington, P. Rez, I. P. Grant and C. J. Humphreys, *Phys. Rev. B: Condens. Matter Mater. Phys.*, 1986, **34**, 1467.
33 E. Stavitski and F. M. F. de Groot, *Micron*, 2010, **41**, 687.
34 A. Uldry, F. Vernay and B. Delley, *Phys. Rev. B: Condens. Matter Mater. Phys.*, 2012, **85**, 125133.
35 I. Josefsson, K. Kunnus, S. Schreck, A. Föhlish, F. de Groot, P. Wernet and M. Odelius, *J. Phys. Chem. Lett.*, 2012, **3**, 3565.
36 M. G. Brik, *J. Phys. Chem. Solids*, 2008, **69**, 2568.
37 M. Stener, G. Fronzoni and M. de Simone, *Chem. Phys. Lett.*, 2003, **373**, 115.
38 J. Fernandez-Rodriguez, B. Toby and M. van Veenendaal, *J. Electron Spectrosc. Relat. Phenom.*, 2015, **202**, 81.
39 H. Ikeno, T. Mizoguchi and I. Tanaka, *Phys. Rev. B: Condens. Matter Mater. Phys.*, 2011, **83**, 155107.
40 M. W. Haverkort, M. Zwierzycki and O. K. Andersen, *Phys. Rev. B: Condens. Matter Mater. Phys.*, 2012, **85**, 165113.
41 J. C. Slater, *Phys. Rev.*, 1929, **34**, 1293.
42 R. D. Cowan, *The Theory of Atomic Structure and Spectra*, University of California Press, Berkeley, 1981.
43 B. G. Wybourne, *Phys. Rev.*, 1966, **148**, 317.
44 S. H. Vosko, L. Wilk and M. Nusair, *Can. J. Phys.*, 1980, **58**, 1200.
45 J. P. Perdew, K. Burke and M. Ernzerhof, *Phys. Rev. Lett.*, 1996, **77**, 3865.
46 P. J. Stephens, F. J. Devlin, C. F. Chabalowski and M. J. Frisch, *J. Phys. Chem.*, 1994, **98**, 11623.
47 E. Van Lenthe and E. J. Baerends, *J. Comput. Chem.*, 2003, **24**, 1142.
48 F. Neese and E. I. Solomon, *Inorg. Chem.*, 1998, **37**, 6568.
49 F. M. F. de Groot, J. C. Fuggle, B. T. Thole and G. A. Sawatzky, *Phys. Rev. B: Condens. Matter Mater. Phys.*, 1990, **41**, 928.
50 T. Uozumi, K. Ojkada, A. Kotani, R. Zimmermann, P. Steiner, S. Hüfner, Y. Tezuka and S. Shin, *J. Electron Spectrosc. Relat. Phenom.*, 1997, **83**, 9.
51 F. M. F. de Groot, J. C. Fuggle, B. T. Thole and G. A. Sawatzky, *Phys. Rev. B: Condens. Matter Mater. Phys.*, 1990, **42**, 5459.
52 J. S. Griffith, *The Theory of Transition-Metal Ions*, Cambridge University Press, Cambridge, 1961.
53 C. Chang, M. Pelissier and P. Durand, *Phys. Scr.*, 1986, **34**, 394.
54 E. van Lenthe, E. J. Baerends and J. G. Snijders, *J. Chem. Phys.*, 1993, **99**, 4597.
55 E. van Lenthe, E. J. Baerends and J. G. Snijders, *J. Chem. Phys.*, 1994, **101**, 9783.
56 M. O. Krause and J. H. Olivier, *J. Phys. Chem. Ref. Data*, 1979, **8**, 329.
57 T. Yanai, D. P. Tew and N. C. Handy, *Chem. Phys. Lett.*, 2004, **393**, 51.
58 D. J. Tozer, R. D. Amos, N. C. Handy, B. O. Roos and L. Serrano-Andres, *Mol. Phys.*, 1999, **97**, 859.
59 N. Schmidt, R. Fink and W. Hieringer, *J. Chem. Phys.*, 2010, **133**, 054703.
60 Y. Uehara, D. W. Lindle, T. A. Callcott, L. T. Terminello, F. J. Himpsel, D. L. Ederer, J. H. Underwood, E. M. Gullikson and R. C. C. Perera, *Appl. Phys. A: Mater. Sci. Process.*, 1997, **65**, 179.
61 S. P. Cramer, F. M. F. de Groot, Y. Ma, C. T. Chen, F. Sette, C. A. Kipke, D. M. Eichhorn, M. K. Chan, W. H. Armstrong, E. Libby, G. Christou, S. Brooker, V. Mckee, O. C. Mullins and J. C. Fuggle, *J. Am. Chem. Soc.*, 1991, **113**, 7937.
62 Y. A. Abramov, V. G. Tsirelson, V. E. Zavodnik, S. A. Ivanov and I. D. Brown, *Acta Crystallogr., Sect. B: Struct. Sci.*, 1995, **51**, 942.
63 Y. Wan-Lun and Z. Min-Guang, *J. Phys. C: Solid State Phys.*, 1985, **18**, L1087.
64 P. Dufek, K. Schwarz and P. Blaha, *Phys. Rev. B: Condens. Matter Mater. Phys.*, 1993, **48**, 12672.
65 H. Ramanantoanina, W. Urland, F. Cimpoesu and C. Daul, *Phys. Chem. Chem. Phys.*, 2014, **16**, 12282.
66 H. Ramanantoanina, W. Urland, B. Herden, F. Cimpoesu and C. Daul, *Phys. Chem. Chem. Phys.*, 2015, **17**, 9116.
67 M. Abbate, F. M. F. de Groot, J. C. Fuggle, A. Fujimori, Y. Tokura, Y. Fujishima, O. Strebel, M. Domke, G. Kaindl, J. van Elp, B. T. Thole, G. A. Sawatzky and M. Sacchi, *Phys. Rev. B: Condens. Matter Mater. Phys.*, 1991, **44**, 5419.
68 V. Weber, C. Daul and R. Baltensperger, *Comput. Phys. Commun.*, 2004, **163**, 133.
69 C. K. Jørgensen, *Struct. Bonding*, 1966, **1**, 3.
70 C. E. Schäffer and C. K. Jørgensen, *J. Inorg. Nucl. Chem.*, 1958, **8**, 143.